The thermodynamic effects of solute on void nucleation in Mg alloys

Vicente Munizaga $^{1, a)}$ and Michael L. Falk $^{1, 2, 3, 4, b)}$

- ¹⁾Department of Physics and Astronomy, Johns Hopkins University, Baltimore, MD 21218, USA
- ²⁾ Department of Materials Science and Engineering, Johns Hopkins University, Baltimore, MD 21218, USA
- ³⁾ Hopkins Extreme Materials Institute, Johns Hopkins University, Baltimore, MD 21218, USA
- ⁴⁾ Department of Mechanical Engineering, Johns Hopkins University, Baltimore, MD 21218, USA

(Dated: 31 July 2024)

Replica Exchange Transition Interface Sampling simulations in Mg-Al alloys with high vacancy concentrations indicate that the presence of solute reduces thermodynamic barriers to the clustering of vacancies and the formation of voids. The emergence of local minima in the free energy along the reaction coordinate suggests that void formation may become a multi-step process in the presence of solute. In this scenario, vacancies agglomerate with solute before they coalesce into a stable void with well-defined internal surfaces. The emergence of vacancy-solute clusters as intermediate states would imply that classical nucleation theory is unlikely to adequately describe void formation in alloys at high vacancy concentrations, a likely precursor for alloy strengthening through nanoscale precipitation.

I. INTRODUCTION

Solid state precipitation and growth of new phases inside solid solutions is an important part of the design and manufacturing of metallic alloys. Intermetallic precipitates are one of the most effective methods to strengthen metals because such precipitates often resist dislocation motion. As a result, the alloy strength and failure resistance can be improved^{1,2}. Particularly, for lightweight materials such as Mg and Al alloys, precipitation processing can result in materials suitable for applications in aerospace, automobile, and defense systems^{3–5}.

One optimal microstructure for improving the strength of metals involves a high density of small precipitates. Recent studies have demonstrated that this microstructure can be induced in Mg alloys through mechanical deformation⁶. It is hypothesized that this microstructure arises due to the high densities of defects, particularly vacancies and voids that are commonly found at elevated concentrations after severe plastic deformation⁷. Voids and vacancy-solute clusters may play crucial roles in the nucleation of intermetallic precipitates, but the mechanism for this effect remains poorly characterized. Clustering may serve as a meta-stable precursor to the formation of intermetallic nuclei, particularly under non-equilibrium conditions.

Voids can act as sites for heterogeneous precipitation due to their internal surfaces, which reduce energy barriers associated with the formation of precipitates. Additionally, voids exhibit stability over a range of temperatures⁸, and they can interact with other defects, capturing or emitting vacancies. This interaction

may contribute to the diffusion of solute, crucial for the nucleation and growth of new phases. These defects have been studied in the context of radiation damage^{9–12}, where understanding void nucleation is critical for ensuring the long-term reliability of materials in a radiation environment. As stable voids accumulate due to radiation damage, their rapid growth under irradiation can induce substantial changes in material properties. However, in the present work, we are interested in vacancy clustering only due to an excess of vacancies in presence of solute, differing from the context of radiation, where radiation dosage, interaction with interstitials, and dislocations are important factors¹³.

The interaction of solute with voids warrants deeper consideration. While it is generally well-understood that an excess of vacancies promotes solute diffusion, Wu et al. 14 reported that a high density of vacancies can pin solute atoms. It is known that voids can alter the composition in their vicinity by attracting or repelling solute atoms 15, which could promote or suppress the nucleation of precipitates. Moreover, Yi et al. 16 used atomistic simulations to demonstrate that vacancy clusters induce solute segregation/depletion. In this process, solute atoms also serve to stabilize the vacancy clusters, potentially increasing the lifetimes of vacancy clusters. This enhancement could make them more effective as heterogeneous sites for solute clustering and subsequent precipitation of new phases.

On the other hand, the formation of voids via the agglomeration of vacancies is itself a nucleation process that is not fully understood. Current models assume that voids nucleate from a uniform concentration of vacancies^{17–20}. However, in molecular dynamics (MD) simulations, we have observed that clusters of vacancies could remain locally stable before creating a well-defined internal surface. This suggests that under some conditions, the nucleation of a void with a defined internal

a) vpmuniza@jhu.edu

b) mfalk@jhu.edu

surface could involve a multi-step process. Fluctuations in the density of excess vacancies may lead to small aggregates that must spontaneously grow beyond a critical size before they can coalesce into a stable void²¹.

One noteworthy observation is the impact of the local depletion of vacancies on the creation of an internal surface. Our simulations reveal that the nucleation of an internal surface surpasses the diffusion of vacancies, resulting in local depletion during the rapid nucleation process. This effect has been reported previously for nucleation in dense fluid systems and the nucleation of voids^{22,23} but has not received widespread consideration.

Void nucleation under such conditions is a "rare event," taking place on time scales much longer than a typical molecular vibrational period due to the high free energy barrier between the initial and final states. This makes MD very inefficient for exploring the kinetics of such processes. To overcome this problem, an advanced simulation technique is required to study the transition event such as umbrella sampling²⁴, metadynamics²⁵, or hyperdynamics²⁶. However, if the order parameter or "boost potential" is not correctly chosen, such simulations can result in a poor estimation of the free energy barrier. Simulations based on trajectories such Transition Path Sampling (TPS) and Transition Interface Sampling (TIS) aim to solve this problem by generating statistical ensembles of dynamic pathways between the initial and final states.

TPS simulations perform a Monte Carlo sampling of trajectories in the phase space. By using a shooting algorithm²⁷, TPS generates new pathways (or trajectories) from an existing initial trajectory. Each new pathway is accepted or rejected, preserving detailed balance. The collection of pathways provides insight into the mechanisms of the transition and enables the computation of rate constants. In the same spirit, the TIS methodology introduces to the path sampling a progress parameter to define a set of hypersurfaces in the phase space between the metastable states²⁸. These so-called "interfaces" are used to define crossing probabilities, which improve the computation of rate constants. TIS simulations and their variations have been applied in the contexts of protein folding 29,30 , chemical reactions 31 , nucleation $^{32-34}$ and solid-solid transformation in nanocrystals under pressure³⁵. Only recently have these methods been applied to studying the nucleation of solid-solid phase transitions in bulk crystals, particularly displacive transitions in the absence of chemical reordering 36 .

An interesting extension of TIS is the Replica Exchange Transition Interface Sampling (RETIS)³⁷. In RETIS each interface defines a replica, and paths are sampled for each replica using TIS moves. This extension also includes a swapping move between replicas that reduces the correlation between the paths generated. In addition, RETIS defines a new ensemble that consists of trajectories that explore the reactant state. This allows direct computation of the flux through the boundary of

the reactant state.

This study focuses on examining the mechanism of void nucleation, particularly the role of vacancies and the influence of solute, utilizing molecular dynamics (MD) simulations within the RETIS approach. Our specific investigation centers on Mg-Al alloys, with a 5 at. % Al concentration, and we compare them to pure Mg. The systems under scrutiny are characterized by a fixed number of vacancies, providing insights into the clustering behavior of excess vacancies within the grain, away from grain boundaries, and absent external sources or sinks. Our primary interest lies in addressing how an excess of vacancies clusters in the presence of solute by comparing the same system with and without solute under identical conditions.

With a fixed number of excess vacancies, the system exhibits reversible transitions between vacancies and voids, particularly in regions with local depletion. As mentioned earlier, depleted regions around growing crystalline nuclei are observed in real-world scenarios when compositional homogenization does not occur quickly enough to align with the Classical Nucleation Theory (CNT) assumption of constant background supersaturation. While our simulations align more closely with this real-world scenario, they deviate from the assumptions of CNT³⁸.

II. METHODS

A. Molecular dynamics simulations

Rare event simulations such as RETIS, require an initial pathway and a progress coordinate. The purpose of the initial path is to serve as a starting point for generating trajectories, but the particular choice of the initial path must not influence the converged statistics. In this work, the progress coordinate λ for characterizing the transition is given by

$$\lambda = \left(\frac{\varphi_{mean} - \varphi_{min}}{\varphi_{mean}}\right),\tag{1}$$

where φ_{mean} and φ_{min} statistically approximate the average particle density of the system and the minimum local particle density of the system, respectively. The average particle density is approximately constant, while the minimum local particle density decreases as vacancies agglomerate. Therefore, λ is close to zero when vacancies are dispersed throughout the system and approaches one when vacancies agglomerate. The local particle density is calculated for each MD step as

$$\varphi(\vec{r}) = \sum_{\alpha=1}^{N} \eta(|\vec{r}^{\alpha} - \vec{r}|), \tag{2}$$

where α is a label for each particle and $\eta(r)$ is a weighting function, defined on a volume V such that

$$\int \eta dV = 1. \tag{3}$$

The function $\eta(r)$ used in this work is

$$\eta(r) = \left\{ \begin{array}{l} \frac{3\pi}{4R^3(\pi^2 - 6)} \left(1 + \cos\left(\frac{\pi r}{R}\right) \right), & \text{if } r \le R \\ 0, & \text{if } r > R \end{array} \right\}, \quad (4)$$

where the length-scale on which the density is measured is defined by setting R=10Å. Using this value we are able to distinguish the transition from dispersed vacancies to the agglomeration into a void. Because $\eta(r)$ is just a function of r, $dV\equiv 4\pi r^2\text{dr}$. All calculations for densities in this work are performed using Equations 2 and 4. We create a grid of 20x20x20 points in the simulation box, and at each point, we compute the local density φ . We determine the minimum local density φ_{min} and the average φ_{mean} from the local values of φ . We note that φ_{mean} arises from a sampling of the density in the box. Even in the presence of the largest void in our simulations, φ_{mean} is almost identical to the average box density defined as number of atoms divided by the volume of the box.

Paths are generated using the open package LAMMPS³⁹ and a modified embedded-atom method (MEAM)⁴⁰ potential for the MgAl system. This MEAM potential accurately predicts many of the structural properties of pure Mg and the Mg-Al binary system including the bulk modulus, point defects, planar defects, and thermal properties. Equations of motion in MD are integrated using a Verlet algorithm⁴¹, and the integration time step dt is chosen to be 1fs. A Nosé-Hoover thermo-barostat^{42–44}, is used to maintain the temperature and pressure, with thermostatting and barostatting time constants of 0.1 ps and 1 ps, respectively.

To obtain the initial path, we induce the system to undergo the transition of interest by introducing a uniform strain into the simulation box. We create a periodic simulation box with a side length of approximately 58Å containing an hcp crystal with 8000 atoms of which 0.5\% are randomly removed to create randomly dispersed vacancies. Of the 7960 remaining atoms, 5% are randomly chosen to be Al atoms. This system size is similar to the one used by Yi et al. 16 for studying the diffusion of vacancy clusters, and the vacancy concentration is close in magnitude to that reported by Wu et al. in their experimental study¹⁴. Initially, the box is equilibrated in the NPT ensemble at temperature T = 600 K, and all components of the stress tensor are set equal to zero. Strain is imposed by isotropically stretching the box by 4% and rescaling the atom positions. While keeping the volume constant, the temperature is increased to 700 K to enhance diffusion for 1 ns. Subsequently, the temperature is reduced back to 600 K and kept constant for 50 ns of simulation time, during which nucleation occurs.

The strain increases vacancy mobility and the diffusion of solute as well as making void formation energetically favorable, inducing the desired transition.

The above procedure was used to generate ten independent simulations to mitigate the bias that could be introduced by spawning trajectories from a single path. Figure 1 shows the reaction coordinate for these ten different pathways as a function of time. The trajectories correspond to voids nucleating at different locations in the simulation box. Figure 2, shows the vacancies and voids in red and the distribution of solute in blue, for four of these paths. We observe that the distribution of solute for each path is different. In this work, one pathway is used per replica as an initial trajectory.

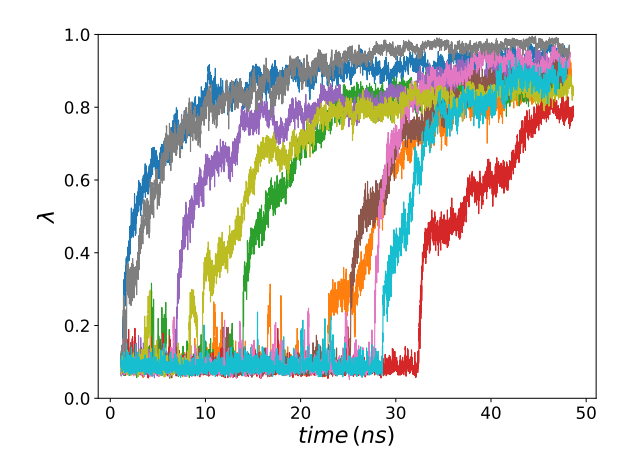


FIG. 1. The evolution of the progression parameter λ in the ten initial pathways for Mg-Al with 4% imposed strain at T = 600 K.

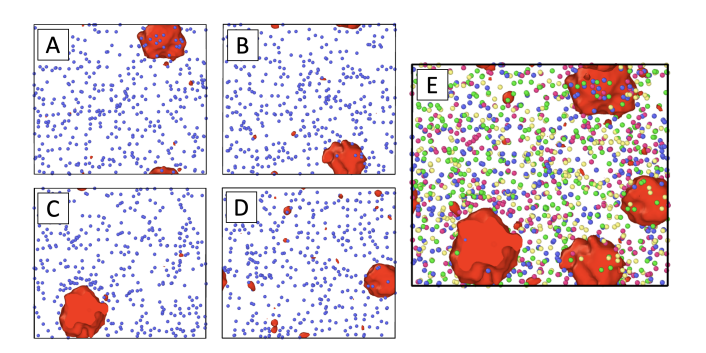


FIG. 2. Panels A, B, C, and D visualize the vacancies and voids (red), and solute (blue) for four independent simulations among the ten generated. Figure E, is a superposition of all images, where the solute is presented with different colors to show that the pathways are decorrelated and have different distributions of solute. Images are generated using the surface mesh algorithm implemented in OVITO⁴⁵.

After the initial trajectories are generated in the strained configuration, an affine transformation is applied to all frames along each path in order to create

unstrained trajectories. Thereafter, we perform a quick relaxation of the atom positions in each frame by using MD to simulate the time evolution of each frame for 2 ps. During this relaxation the temperature is maintained at 600 K and all the stress tensor components are maintained at zero. In this manner, a set of states along the transition path are created by storing the last frame of each relaxation run.

The configurations generated using the procedure described above do not correspond to a set of time-sequenced frames as would be generated by an integrator in an MD simulation. However, we use these configurations to generate the "shooting moves" in the RETIS simulation, i.e. new trajectories are generated that evolve physically in the phase space originating from these configurations³⁶. All these resulting MD-generated pathways are simulated in the NPT ensemble at various temperatures while maintaining all the components of the stress tensor at zero.

For pure Mg, we followed the same steps, with the same number of atoms and vacancy concentration. However, in order to achieve the transition for each pathway, we applied a strain equal to 5.4 %.

B. Path analysis

A path or trajectory in TIS is a sequence of frames $\mathbf{x}(\tau) = \{x_0, x_1, x_2, ..., x_L\}$ where each x_i is a point in the phase space. The length L of the path is measured in time steps and satisfies $\tau = L\Delta t$, where Δt is the time between these frames and τ is the total duration of the trajectory. The probability of creating a sequence of duration τ is given by

$$\pi\left[\mathbf{x}(\tau)\right] = \rho(\mathbf{x}_0) \prod_{i=0}^{L-1} p(x_i \to x_{i+1}), \tag{5}$$

where $\rho(\mathbf{x}_0)$ is the ensemble distribution and $p(x_i \to x_{i+1})$ is the probability for the sequence to go from x_i to x_{i+1} . In the case of MD, $p(x_i \to x_{i+1})$ can be calculated as

$$p(x_i \to x_{i+1}) = \delta [x_{i+1} - \phi(x_i)]$$
 (6)

where $\phi(x_i)$ is the MD propagator applied to the configuration x_i . In this manner, the probability of finding a path can be obtained as

$$\mathcal{P}\left[\mathbf{x}(\tau)\right] = \pi \left[\mathbf{x}(\tau)\right] / Z,\tag{7}$$

with Z being a normalization constant analogous to the partition function, defined as

$$Z = \int \mathcal{D}\mathbf{x}\pi \left[\mathbf{x}\right],\tag{8}$$

where the integral runs over all possible paths and all lengths. In the context of MD, it is possible to write the

last integral as⁴⁶

$$Z = \int dx_0 \rho(x_0), \tag{9}$$

that runs over all initial configurations of all possible paths.

In TIS, the interfaces are a sequence of values of the progression parameter along the phase space $\lambda_0, \lambda_1, ..., \lambda_n$, where λ_0 is the boundary of state A, and λ_n is the boundary of B. The trajectories generated can be grouped in ensembles depending on the interface they have crossed. Therefore, the path ensemble $A\Lambda_i$ is defined as all paths that start at A, end at B, or return to A, provided that they have crossed the interface λ_i .

A finite number of paths are collected for each ensemble, and we desire to obtain the best estimation of the path probability. To achieve this, we have to estimate the so-called complete path ensemble probability $\mathcal{P}_c[\mathbf{x}]$, proposed by Rogal *et al.*⁴⁷.

For each ensemble, the crossing probability is defined as

$$P(\lambda|\lambda_i) = \int \mathcal{D}\mathbf{x} \mathcal{P}_{A\Lambda_i} \left[\mathbf{x}\right] \theta(\lambda_{max} \left[\mathbf{x}\right] - \lambda)$$
 (10)

with $\mathcal{P}_{A\Lambda_i}[\mathbf{x}]$ the path probability on the ensemble $A\Lambda_i$. θ is the Heaviside step function, and $\lambda_{max}[\mathbf{x}]$ is the maximum value of λ on the path \mathbf{x} . For the reverse process, the ensembles and crossing probabilities are defined similarly. We can compute the crossing probabilities for each ensemble $A\Lambda_0, A\Lambda_1, ..., A\Lambda_{n-1}$ and merge them using appropriate weights by applying the weighted histogram analysis method (WHAM)⁴⁸. In TIS, the weights for each crossing probability are $w_i = 1/\sum_{j=0}^i \left(Z_A/Z_{A\Lambda_j}\right)$, with Z_A involving all paths that leave the state A.

Using the weights for the process $A \to B$ and $B \to A$ we can re-weight each ensemble and estimate the complete path ensemble probability $\mathcal{P}_c[\mathbf{x}]$, necessary for the estimation of important physical properties of the transition. The free energy of the transition can be estimated as

$$\Delta \mathcal{F}(\lambda) = -k_B T \ln[\rho(\lambda)], \tag{11}$$

where $\rho(\lambda)$ is the probability density of states, given by

$$\rho(\lambda) = C \int \mathcal{D}\mathbf{x} \sum_{k=0}^{L} \prod_{i}^{m} \delta\left(\lambda^{(i)}(x_{k}) - \lambda^{(i)}\right) \mathcal{P}_{c}\left[\mathbf{x}\right] \quad (12)$$

The expression above is valid for an m-dimensional progression parameter λ , where C is a normalization constant. In this work λ is one-dimensional and it is related to the local atomic density, as described above.

C. Rare event simulations

To sample the transition between the state characterized by dispersed vacancies and the state with a void,

we carried out RETIS simulations. We modified the open package PyRETIS⁴⁹ to enable the propagation of pathways in the NPT ensemble using LAMMPS. This requires the subsequent statistical analysis to take into account the relative statistical probability of paths that start from states of differing initial volumes in the NPT ensemble, as described below.

In RETIS, the progress coordinate λ defines a set of hypersurfaces λ_i between two metastable states, state A for $\lambda < \lambda_A$ and state B for $\lambda > \lambda_B$, such that $\lambda_A < \lambda_i < \lambda_B$. For each interface λ_i , an ensemble of trajectories is generated and collected using Monte Carlo (MC) moves for the A \rightarrow B and B \rightarrow A process. In our investigation, pathways are harvested using a combination of 50% swapping moves and 50% shooting moves. The latter moves generate new trajectories by randomization of the atomic velocities and the volume, according to the NPT ensemble⁵⁰.

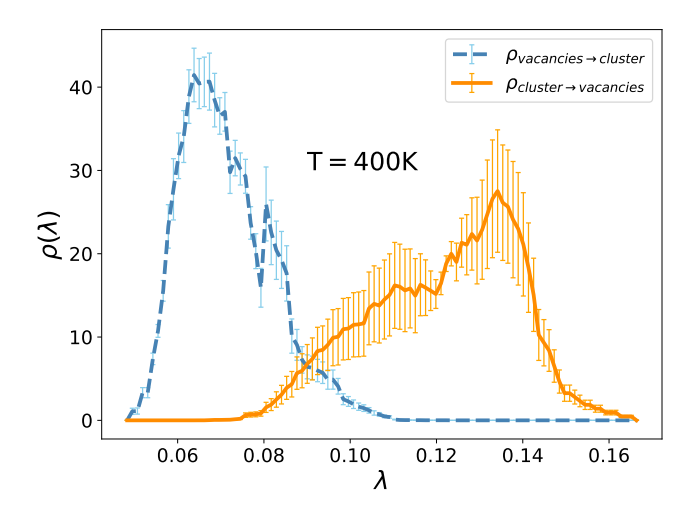


FIG. 3. Conditional probability density of states for vacancies \rightarrow cluster (blue) and cluster \rightarrow vacancies (orange) transitions in Mg-Al at 400 K. The labels vacancies \rightarrow cluster and cluster \rightarrow vacancies indicate the transitions from which the data were extracted. Error bars are based on a single standard deviation.

Determining the existence of meta-stable states involves a trial-and-error process. We analyze the conditional probability density of states for known transitions and adjust these boundaries to achieve convergence. These probabilities are conditional in the sense that the states collected from the forward process $A \rightarrow B$ include paths that within state A as well as those that emerge from A, whether they reach B or return to A. They exclude paths that originate from B. The same definition applies for the reverse process $B \rightarrow A$. The resulting probabilities are proportional to the number of states visited for all paths and are calculated for each transition analyzed. They provide insight into the parameter regimes of meta-stable states.

Analysis of these conditional probability densities reveals the existence of basins between vacancies and the

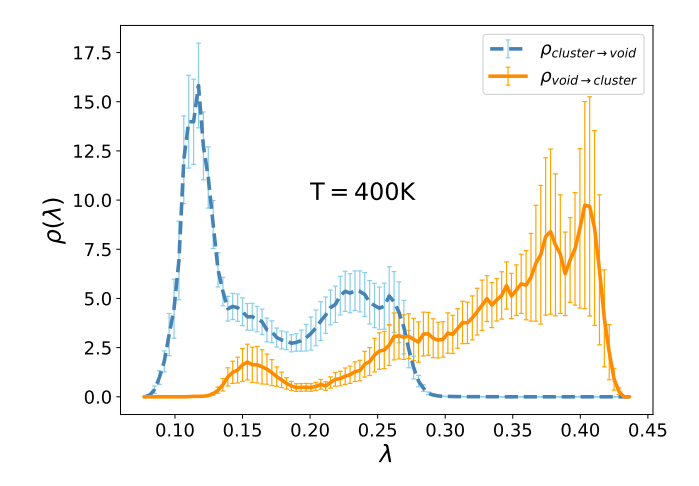


FIG. 4. Conditional probability density of states for cluster \rightarrow void (blue) and void \rightarrow cluster (orange) in Mg-Al at 400 K. The labels cluster \rightarrow void and void \rightarrow cluster indicate the transitions from which the data were extracted. Error bars are based on a single standard deviation.

void where paths become trapped for extended periods during simulations. Consequently, simulations from vacancies to voids were conducted in two stages: vacancies-cluster and cluster-void, each one for the forward (AB) and backward transition (BA). The interfaces used for each simulation are detailed in Table I.

Figure 3 presents the conditional probability density of states for the vacancies \rightarrow cluster (AB process) and cluster \rightarrow vacancies (BA process) simulations. Each simulation exhibits a distinct peak corresponding to the initial state. Isolated vacancies are discernible in the range of $0.06 < \lambda < 0.08$, while the presence of clusters is evident in the interval $0.11 < \lambda < 0.14$.

Regarding the cluster-void transition, Figure 4 shows the conditional probability density of states for transitions from cluster to void and from void to cluster. Each curve displays a distinct peak corresponding to the metastable states. A cluster of vacancies is evident in the range of $0.11 < \lambda < 0.14$, while a void with a well-defined internal surface is located in the interval $\lambda > 0.30$. Additionally, a third peak is observed in the cluster \rightarrow void transition for $0.20 < \lambda < 0.26$, which could represent another meta-stable cluster state.

The resulting data, shows that the state characterized by dispersed vacancies is described by $\lambda < 0.08$, while the state with a void by $\lambda > 0.30$. Reweighting the simulations is necessary to combine all transition datasets so as to fully understand the contribution of these peaks to the overall probability density distribution for the process. To achieve this, we merge the conditional probability from vacancies \rightarrow cluster and cluster \rightarrow vacancies into one probability density vacancies \leftrightarrow cluster. Similarly, we merge the conditional probability from cluster \rightarrow void and void \rightarrow cluster into one probability density cluster \leftrightarrow void. Finally, we merge the probability densities from vacancies \leftrightarrow cluster and cluster \leftrightarrow void

into vacancies↔void. Below we present the reweighting method for the case of Mg-Al at 400 K; the details for other cases can be found in the supplementary information.

To achieve the properly reweighted probability density, we merge these complementary datasets by imposing detailed balance⁵¹ between two states which we will refer to as A and B, where A and B correspond to either the vacancies state and cluster state respectively, or the cluster state and void state respectively. The merged probability density, which we no longer refer to as conditional, contains information from both the forward and backward processes, being a superposition of the conditional probability densities,

$$\rho(\lambda) = c_A \rho_{AB}(\lambda) + c_B \rho_{BA}(\lambda). \tag{13}$$

Here c_A and c_B are the weights of the superposition that we must estimate. From detailed balance, we know

$$k_{AB}p_A = k_{BA}p_B, (14)$$

where

$$k_{AB} = f_A P(\lambda_B | \lambda_A) \tag{15}$$

is the transition rate constant. Here, f_A represents the flux measuring how often trajectories are initiated at state A, and $P(\lambda_B|\lambda_A)$ is the crossing probability for paths to reach state B before returning to state A. The reverse process follows a similar formulation. The probabilities p_A and p_B denote the probabilities of being in states A and B, respectively. We defined the state A such $\lambda < \lambda_A$ and the state B such $\lambda > \lambda_B$. Therefore the probabilities p_A and p_B are given by

$$p_{A} = \int_{\lambda < \lambda_{A}} \rho(\lambda) d\lambda$$
$$= \int_{\lambda < \lambda_{A}} \left(c_{A} \rho_{AB}(\lambda) + c_{B} \rho_{BA}(\lambda) \right) d\lambda, \tag{16}$$

and

$$p_{B} = \int_{\lambda > \lambda_{B}} \rho(\lambda) d\lambda$$

$$= \int_{\lambda > \lambda_{B}} (c_{A} \rho_{AB}(\lambda) + c_{B} \rho_{BA}(\lambda)) d\lambda.$$
 (17)

Then, using Eq. 14 we determine that

$$\frac{\int_{\lambda < \lambda_A} \left(c_A \rho_{AB}(\lambda) + c_B \rho_{BA}(\lambda) \right) d\lambda}{\int_{\lambda > \lambda_B} \left(c_A \rho_{AB}(\lambda) + c_B \rho_{BA}(\lambda) \right) d\lambda} = \frac{k_{BA}}{k_{AB}}.$$
 (18)

Using Eq. 18 and the normalization of $\rho(\lambda)$ we can solve for c_A and c_B .

As mentioned previously, we consider four transitions. Hence, we have four probability densities to merge: vacancies \rightarrow cluster, cluster \rightarrow vacancies, cluster \rightarrow void, and void \rightarrow cluster. Using the above procedure we can calculate $\rho_{\text{vac}\leftrightarrow\text{cl}}$ and $\rho_{\text{cluster}\leftrightarrow\text{void}}$ from

their corresponding conditional probabilities. To merge these we again apply detailed balance, imposing that

$$k_{\text{vac}\to\text{cl}}k_{\text{cl}\to\text{void}}p_{\text{vac}} = k_{\text{void}\to\text{cl}}k_{\text{cl}\to\text{vac}}p_{\text{void}},$$
 (19)

which results in an overall probability density $\rho_{\text{vac}\leftrightarrow \text{void}}$.

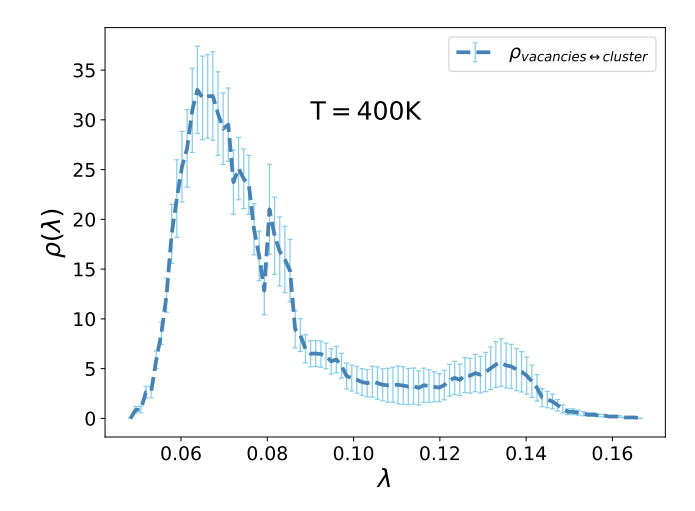


FIG. 5. Merged probability density of states for Mg-Al at 400 K during vacancies \leftrightarrow cluster transition.

In the case of the vacancy-cluster transition in Figure 3, the transition rates are $k_{AB} = (4.84 \pm 1.71) \,\mathrm{ns}^{-1}$ and $k_{BA} = (20.9 \pm 7.3) \,\mathrm{ns}^{-1}$, respectively. The detailed balance condition and normalization imply that, since $k_{AB} < k_{BA}$, the probability density $p_A(\lambda)$ carries greater weight compared to $p_B(\lambda)$. This is reflected by the respective weights $c_A = 0.80 \pm 0.08$ and $c_B = 0.20 \pm 0.08$ and the resulting merged curve presented in Figure 5.

Similarly, for the cluster-void transition in Figure 4, the transition rates for this process are $k_{AB} = (0.368 \pm 0.148) \,\mathrm{ns^{-1}}$ and $k_{BA} = (4.61 \pm 1.69) \,\mathrm{ns^{-1}}$, respectively. The detailed balance condition and normalization imply that $k_{AB} < k_{BA}$, and the probability density $p_A(\lambda)$ carries greater weight compared to $p_B(\lambda)$. This is reflected by the respective weights $c_A = 0.96 \pm 0.02$ and $c_B = 0.04 \pm 0.02$ and the resulting curve presented in Figure 6.

Finally, repeating the process for both the vacancies-cluster and cluster-void presented datasets shown in Figure 7, the overall probability density for vacancies \leftrightarrow void is presented in Figure 8. In this instance, the weights for merging the vacancies \leftrightarrow void and void \leftrightarrow vacancies datasets are $c_A = 0.71 \pm 0.15$ and $c_B = 0.29 \pm 0.15$, respectively.

Figure 8 presents the relationship between ρ and λ for the entire vacancy \leftrightarrow void process. The curve exhibits several distinct peaks located at $\lambda < 0.08$, $0.11 < \lambda < 0.15$, $0.22 < \lambda < 0.26$, and $\lambda > 0.30$ (as shown in the semi-log plot). The first peak corresponds to isolated vacancies, followed by a sequence of intermediate stages of clustering, and, finally, the formation of small voids.

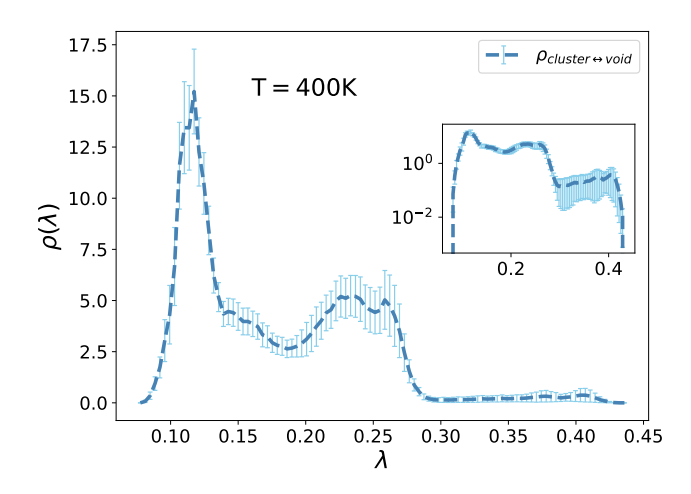


FIG. 6. Merged probability density of states for Mg-Al at 400 K during cluster \leftrightarrow void transition. The plot also provides a semi-log scale visualization of the same data.

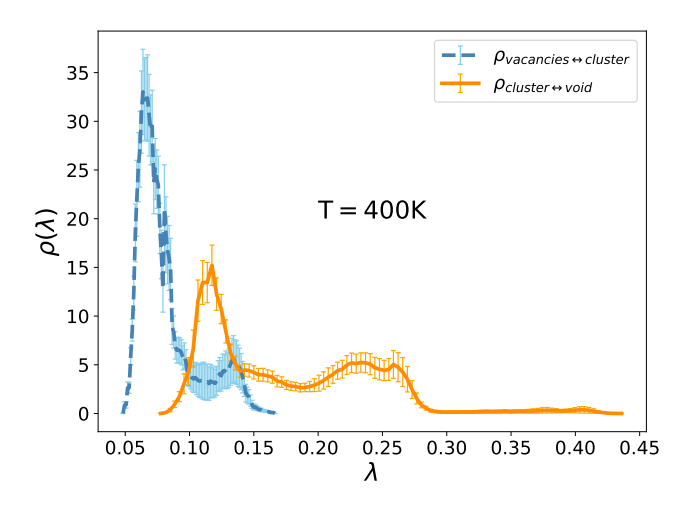


FIG. 7. Probability density of states for vacancies \leftrightarrow cluster (blue) and cluster \leftrightarrow void (orange) in Mg-Al at 400 K. Error bars are based on a single standard deviation

The locations of the hypersurfaces shown in Table I are arbitrary. However, they are typically chosen such that there is at least 10% of superposition between neighboring interfaces⁵². The boundary chosen for the states A and B allows paths to explore the basins long enough before crossing the first interface to ensure decorrelation but short enough to achieve reasonable simulation times, on the order of ns.

In RETIS simulations, path correlation is expected. However, we can reduce this problem by selecting paths at evenly spaced intervals and analyzing the auto-correlation function (ACF) applied to the lengths⁵². To implement this approach, we arranged the paths generated through shooting moves in the order they were

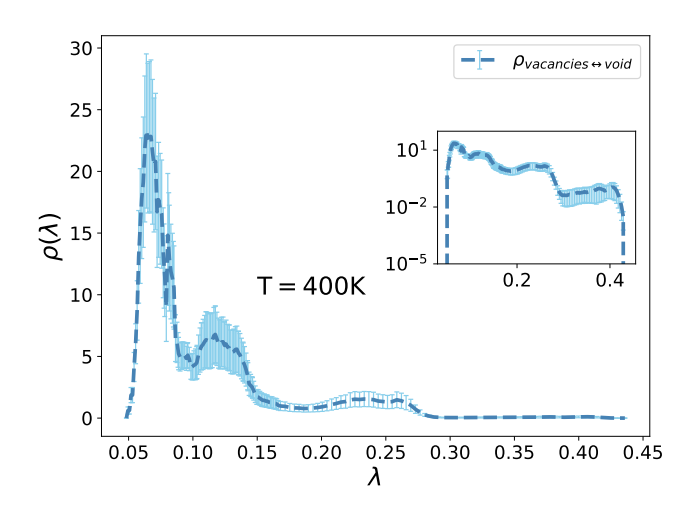


FIG. 8. Probability density of states for vacancies \leftrightarrow cluster (blue) and cluster \leftrightarrow void (orange) in Mg-Al at 400 K. Error bars are based on a single standard deviation

Interfaces (λ_i) : Mg-Al				
Simulation	T = 400 K	T = 500 K	T = 600 K	
vacancies-cluster AB	0.08 - 0.11	0.08 - 0.11	0.08 - 0.11	
cluster-vacancies BA	0.08 - 0.11	0.08 - 0.11	0.08 - 0.11	
cluster-void AB	0.13 - 0.30	0.15 - 0.30	0.15 - 0.30	
void-cluster BA	0.13 - 0.30	0.15 - 0.30	0.15 - 0.30	
Interfaces (λ_i) : Mg				
Simulation	T = 400 K	T = 500 K	T = 600 K	
vacancies-cluster AB	0.08 - 0.11	0.08 - 0.11	0.08 - 0.11	
cluster-vacancies BA	0.08 - 0.11	0.08 - 0.11	0.08 - 0.11	
cluster-void AB	0.20 - 0.30	0.20 - 0.30	0.20 - 0.30	
void-cluster BA	0.20 - 0.30	0.20 - 0.30	0.20 - 0.30	

TABLE I. The first and the last interface used in MgAl and Mg simulations. There are 10 equally separated interfaces between them. AB notation represents $A\rightarrow B$ process, BA represents $B\rightarrow A$ process.

created, and we omitted them at a predetermined lag. By adopting this procedure, we ensured the acquisition of decorrelated trajectories with a 95% confidence level. The lag values for the pathway selection process can be found in the supplementary material.

Another important criterion to consider is the convergence of the simulations through the behavior of the transition rate constant. Once detailed balance is achieved, the crossing probabilities do not depend on the number of paths, implying that k_{AB} does not change with the generation of new pathways. We used this condition as the criterion of convergence. Table II shows the number of paths and acceptance ratio for each simulation that satisfies the condition. Finally, we compute error bars numerically, using the bootstrap method.

Number of paths: Mg-Al				
Simulation	T = 400 K	T = 500 K	T = 600 K	
vacancies-cluster AB	1936 (0.17)	3522 (0.13)	3086 (0.14)	
cluster-vacancies BA	2761 (0.12)	3379 (0.12)	4459 (0.12)	
cluster-void AB	2330 (0.14)	3535 (0.12)	2974 (0.12)	
void-cluster BA	2550 (0.07)	4499 (0.06)	9666 (0.03)	
Number of paths : Mg				
Simulation	T = 400 K	T = 500 K	T = 600 K	
vacancies-cluster AB	3728 (0.13)	3484 (0.13)	6123 (0.11)	
cluster-vacancies BA	3298 (0.13)	1500 (0.15)	1768 (0.15)	
cluster-void AB	443 (0.13)	2100 (0.17)	4549 (0.15)	
void-cluster BA	1007 (0.11)	2323 (0.09)	7605 (0.04)	

TABLE II. The number of accepted paths generated by shooting moves, used in the analysis for Mg-Al and Mg simulations. AB notation represents $A \rightarrow B$ process, BA represents $B \rightarrow A$ process. The value within the parentheses corresponds to the acceptance ratio for the paths.

III. RESULTS AND DISCUSSION

Usually, vacancies and vacancy clusters are identified by comparing the defective crystal to a perfect structure, achieved by matching atom positions ¹⁶. However, this approach is limited to systems where there is no local change in the crystal structure. Additionally, due to thermal fluctuations, the comparison between the crystals must be preceded by a post-processing technique. A problem with this approach is that such manipulations may eliminate entropy contributions to the free energy and potentially create artificial internal surfaces for small clusters of vacancies.

To address these limitations, we introduce a progression parameter λ , as defined in equation (1), which serves as an indirect measure of the biggest cluster size through the local density. An increase in the value of λ indicates the clustering of vacancies into a void. In this manner, we can naturally follow the evolution of the system during the clustering process within the time of simulation itself. To estimate the number of vacancies present within a cluster, we conducted separate simulations featuring a single nano-void of size N_v positioned at the center. Subsequently, we calculated the corresponding value of λ for each N_v size by averaging over the configurations from ensembles simulated at different temperatures. Figure 9 displays λ as a function of the number of vacancies N_v in such an Mg-Al simulation at 400 K, 500 K, and 600 K. The relationship between the cluster size and λ appears to be nearly monotonic, i.e. one-to-one, to within the error of the calculation. The difference between these curves in Mg-Al and pure Mg is negligible due to the similar atomic volumes of Mg and Al atoms. λ varies approximately linearly with N_v , and the fluctuation in the shape of the cluster increases with temperature, affecting the value of the local density. Consequently, the size of the error bars increases with temperature. It is

worth noting that the progression parameter, λ , provides equivalent information to the largest cluster size commonly used in nucleation studies, yet proves to be easier to track during simulations.

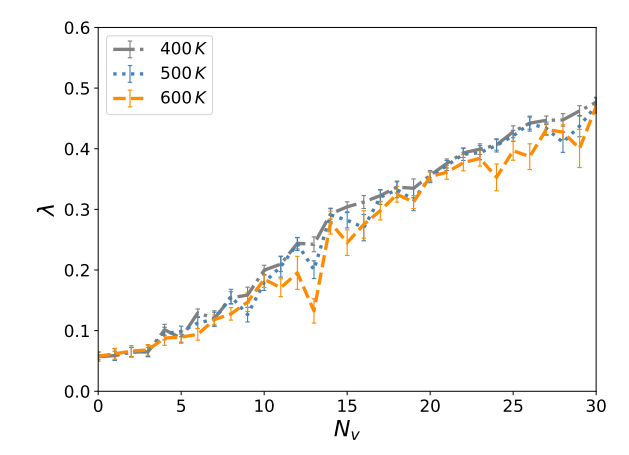


FIG. 9. The progression parameter λ as a function of number of vacancies N_v . The number of vacancies corresponds to an equivalent compact cluster size.

Using the surface mesh algorithm implemented in $OVITO^{45}$, we construct visualizations from distinct stages of the transition at 400 K in Mg-Al, as depicted in Figure 10. These images, along with Fig. 9, offer insights into the stages and sizes of vacancy aggregates during the void nucleation process. The intervals presented here will be further explained later once we compute the free energy. Here, we provide visualizations of the relevant clustering stages.

In the interval $\lambda < 0.08$ (represented by $\lambda \approx 0.07$), we observe a collection of states where vacancies and divacancies are randomly dispersed. Moving to the interval $0.11 < \lambda < 0.14$ (represented by $\lambda \approx 0.12$), we witness an early stage of clustering where the largest cluster has a size of $N_v \approx 6$ vacancies. Vacancies are frequently close to each other, forming di- and tri-vacancies, but no void is evident.

Upon further visualization of the system within the interval $0.22 < \lambda < 0.26$ (at $\lambda \approx 0.24$), we observe a second stage of clustering. During this stage, vacancies form a structure resembling a void, although the internal surface and shape are not fully developed. Finally, at $0.30 < \lambda$, we can observe a void with size $N_v \approx 19$ and a well-defined internal surface

These results suggest that the formation of a void may involve one or more distinct stages, clustering events that progressively achieve a critical size at which the void can develop an internal surface.

Figure 11 illustrates the average local concentration of solute as a function of local density for all frames collected during the path sampling, encompassing both basins and transitions. The ensemble average is performed for all configurations of solute atoms present

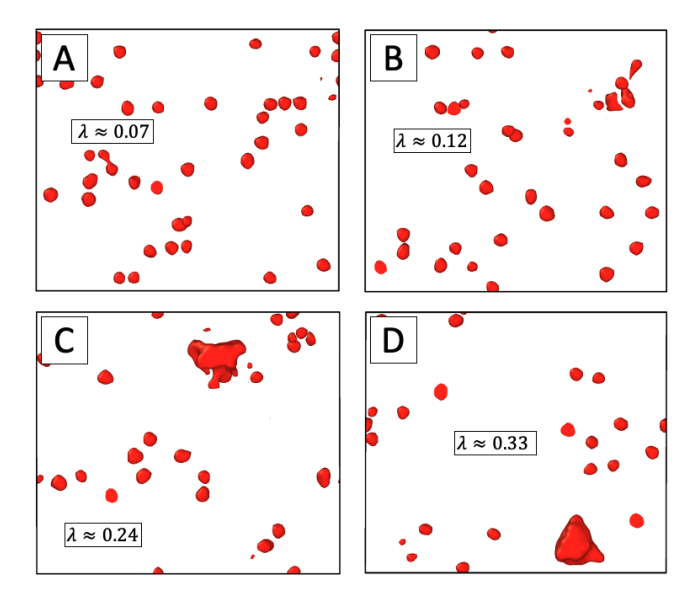


FIG. 10. Figures A, B, C, and D display visualizations of the process of clustering with values of λ at different stages of the void nucleation process drawn from our simulations at 400 K. (A) shows vacancies dispersed randomly when $\lambda \approx 0.07$, (B) displays the presence of clustering when $\lambda \approx 0.12$, (C) shows a structure between a cluster and a void with no well-defined internal surface when $\lambda \approx 0.24$, and (D) shows a void with an internal surface when $\lambda \approx 0.33$.

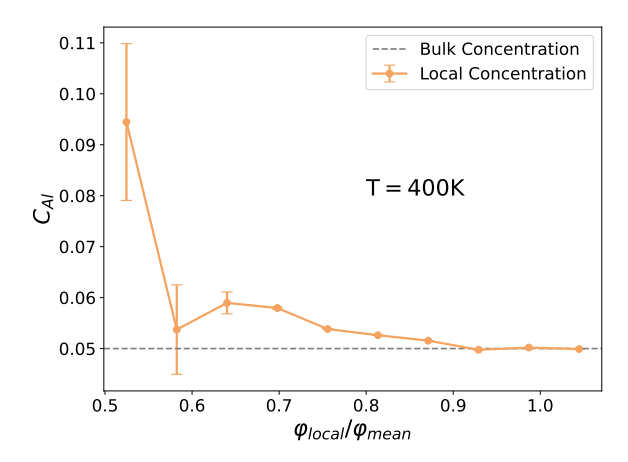


FIG. 11. Local solute concentration v/s local density in Mg-Al at $T=400~\mathrm{K}$ extracted from the accepted paths. Error bars are based on a single standard deviation

during the preparation of the system. In each frame from all paths, the local density is measured at all of the grid points and divided by the average density. At each point, we also compute the local solute concentration. We group the values of the local solute concentration at a given $\varphi_{local}/\varphi_{mean}$ and average those values to construct a histogram of the average solute concentration as a function of the relative local density. When

 $\varphi_{local}/\varphi_{mean} < 0.7$, the local region corresponds to a void, whereas for $\varphi_{local}/\varphi_{mean} > 0.92$, the local region is characterized by the presence of vacancies and di-vacancies randomly dispersed. It is evident that as vacancies cluster to form a void, the local concentration of Al presents a noticeable increase. This implies that there is favorable binding between small voids and solute, which aligns with the findings of Yi et al. ¹⁶. In that work, the free energy of a system including a vacancy cluster or small void in Mg-Al decreased when solute gathered near the defect. Here we found that, on average, vacancies cluster in regions with higher concentration of solute. These results motivated the computation of the free energy to measure the solute effect on vacancy clustering.

The complete path ensemble probability allows for the computation of the probability density and the variation of the free energy profile along the progression parameter. Figure 12 presents the free energy for Mg-Al alloy as a function of λ at different temperatures. The reference energy for each curve is selected such that the minimum value for the free energy is set to zero. This choice allows for easy comparison of the barrier heights between different curves.

From the figure, we observe that at 600 K there is a local minimum located at $\lambda < 0.08$. For larger values of λ , the free energy monotonically increases reflecting the entropic cost of clustering. Upon lowering the temperature to 500 K, a similar behavior is observed, and the minimum at $\lambda < 0.08$ persists. We also observe that for $0.15 < \lambda < 0.25$, the free energy is slightly higher. For $\lambda < 0.15$ and $\lambda > 0.25$, there is no statistically significant difference between the 500K and 600K cases. In both scenarios, we observed that voids with $\lambda > 0.30$ quickly dissolved into separated vacancies.

At 400 K, we again observe a minimum at $\lambda < 0.08$. A plateau/minimum is observed between $0.11 < \lambda < 0.14$. A second plateau/minimum emerges at $0.22 < \lambda < 0.26$, and a barrier to void nucleation is evident at $\lambda = 0.30$. At this temperature, we estimate the free energy barrier to void formation to be approximately 0.22 (eV). which corresponds to an approximate nucleation rate of $J = (k_{AB} + k_{BA})/V = 6.10 \times 10^{-6} \mathrm{ps}^{-1} \mathrm{nm}^{-3}$. It is noteworthy that during the clustering process, as vacancies aggregate, the system transitions through several plateaus/minima. This progression continues until the clusters reach a critical size, at which point the nucleation of the interface becomes possible.

Figure 13 illustrates the free energy profile of the vacancy clustering process in pure Mg at 400 K. To facilitate comparison with the presence of solute, the curve for Mg-Al at the same temperature is also provided. In pure Mg, we observe the same initial local minimum as in Mg-Al, and the curve remains statistically similar for $\lambda < 0.16$. A notable difference is the absence of a plateau/minimum in the range $0.22 < \lambda < 0.26$ for Mg in contrast to what is observed in the alloy system. Void formation in pure Mg exhibits a higher barrier when compared to Mg-Al.

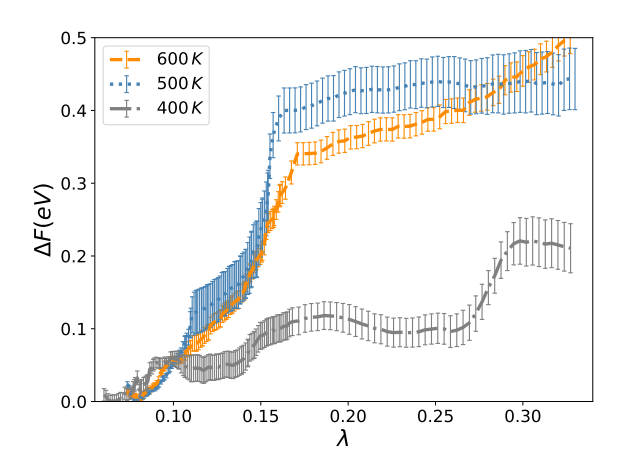


FIG. 12. Free energy as a function of the progression parameter λ for Mg-Al at different temperatures. Error bars are based on a single standard deviation

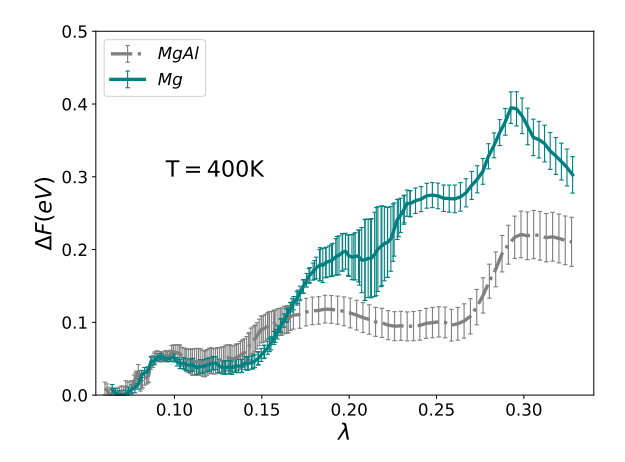


FIG. 13. Free energy as a function of the progression parameter λ for Mg-Al and Mg at T = 400 K. Error bars are based on a single standard deviation

The behavior exhibited by these curves indicates that the introduction of Al solute promotes void formation by lowering the clustering barrier. During the initial stages of clustering, the influence of the solute remains relatively minor, and the initial appearance of a plateau/minimum in both curves at $0.11 < \lambda < 0.14$ can be attributed solely to vacancy-vacancy interactions. As the clusters in Mg-Al gradually find some stability on average within the range of $0.22 < \lambda < 0.26$, they become more predisposed to develop an internal surface, facilitating the void formation process.

Assuming an Arrhenius process between $\lambda < 0.08$ and $\lambda > 0.30$ at 400 K, we computed the attempt frequency ν for $\lambda < 0.08$ and $\lambda > 0.30$ at 400 K. The values are pre-

sented in Table III. We found that the attempt frequency for Mg-Al is decreased by 0.11 ps $^{-1}$, which represents a reduction of $\approx 85\%$ compared to pure Mg. However, this change is within the error, therefore the change is not significant. The transition rate for Mg-Al is significantly higher compared to pure Mg. This suggests that the attempt frequency for reaching $\lambda=0.30$ is not considerably affected by the local minima in $0.22<\lambda<0.26$, and the nucleation process is mainly governed by the reduction of the barrier due to the presence of the solute.

Attempt frequency ν for MgAl (400 K)			
$k_{AB} (10^{-5} \text{ps}^{-1})$	$\nu = k_{AB} \exp(\Delta G/k_B T) (\mathrm{ps}^{-1})$		
$3.82{\pm}1.95$	$0.02{\pm}0.02$		
Attempt frequency ν for Mg (400 K)			
$k_{AB} (10^{-5} \text{ps}^{-1})$	$\nu = k_{AB} \exp(\Delta G/k_B T) (\mathrm{ps}^{-1})$		
0.13±0.10	0.13±0.15		

TABLE III. The table shows the attempt frequency between $\lambda_A = 0.08$ and $\lambda_B = 0.30$ for the A \rightarrow B process.

To assess whether we can reasonably disregard size effects that might arise due to the fixed number of vacancies, we performed an examination of the phenomenon of local depletion upon the nucleation of the void. Ideally, the system simulation box should be big enough to contain the depletion zone around a nucleation site. Taking into account that the vacancy diffusion for pure Mg and Mg-Al using this potential at 450 K is less than $1(\text{Å}^2/\text{ns})^{16}$, the formation of internal surface is constrained by the local concentration of vacancies. Specifically, in our simulations, the nucleation of an internal surface for Mg-Al occurs over a time scale of approximately $\tau = 1/JV \approx 0.87$ ns, whereas the diffusion of vacancies across the entire volume takes about ≈ 561 ns, a process that is three orders of magnitude slower. Solute diffusion is even more limited. In essence, clustering takes place within a background of fixed vacancies and solute.

Figure 14 provides a visual representation of this phenomenon. We selected all frames that contain a critical cluster and computed the local density over the overall density in Mg-Al when vacancies are dispersed. For pure Mg, the behavior is analogous since the atomic species have approximately the same size. On average, local depletion is observed up to 15Å from the nucleation site. The void at this stage has a mean radius of $\approx 6\text{Å}$, resulting in a depletion zone of ≈ 9 Å. Beyond this range, the local density corresponds to that of a crystal with a vacancy concentration of 0.5%. This behavior has been suggested before^{22,23} implying that CNT fails to describe the nucleation of nanovoids. Both the capillarity approximation and the assumption of a constant concentration of vacancies surrounding the cluster during nucleation appear to be violated. Hence, simulations with fixed num-

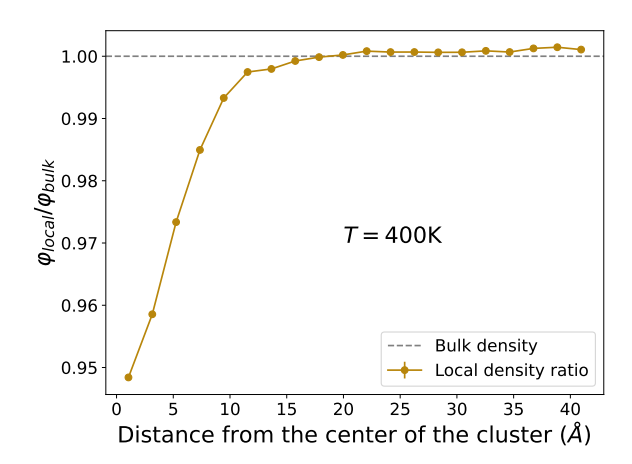


FIG. 14. Local density v/s distance from the center of a critical cluster in Mg-Al at T = 400 K extracted from the accepted paths. This corresponds to the critical region characterized by $0.28 < \lambda < 0.32$

bers of vacancies closer to a real scenario according to Blow $et\ al.^{38}$.

IV. CONCLUSION

Our atomistic simulations using the formalism of Transition Interface Sampling (TIS) provide evidence that void nucleation is thermodynamically favored by the presence of solute in Mg-Al alloys. Plateaus in the free energy profile suggest that the clustering process may involve the formation of intermediate meta-stable structures before the nucleation of a void. However, statistical limitations prevent us from definitively confirming or excluding this behavior. Moreover, our analysis indicates that the presence of solute has a negligible effect on the attempt frequency for nucleating small voids. The enhancement in the nucleation process is primarily driven by the free energy of the transition state. We also found that the concentration of solute increases as vacancies agglomerate into a void.

Our investigation uncovers that vacancy agglomerations are confined by local supersaturation, a consequence of the disparity in time scales between vacancy diffusion and clustering. This establishes an "equilibrium" between void formation and isolated vacancies. Minor shifts in local solute concentration bring about a thermodynamic effect by modifying the free energy barrier for clustering. In Mg-Al, clustering is promoted, suggesting that vacancy clustering and solute precipitation are mutually influential. Modest adjustments in local solute concentration may encourage vacancy clustering, while simultaneously, vacancy clusters and voids induce solute segregation. This observation could explain the zones of solute concentration reported by Yi et al. ¹⁶ and Sasaki et al. ⁵³.

We anticipate that in other alloys, characterized by unfavorable interactions between vacancies and solute, the presence of solute is unlikely to promote void formation. Additionally, our findings suggest that using local density to describe the different stages of vacancy clustering provides an accurate progression parameter for distinguishing void formation stages. This parameter offers the advantage of being potentially measurable in experiments. It also exhibits a nearly monotonic relationship with the number of vacancies that form the biggest cluster — a quantity traditionally used as an order parameter in modeling void nucleation. Further interpretation of this progression parameter will be presented in future work.

V. SUPPLEMENTARY MATERIAL

Please refer to the supplementary material for detailed information regarding the lag values utilized in selecting both forward and backward processes for Mg-Al and pure Mg at temperatures of 400 K, 500 K, and 600 K. Additionally, the supplementary material contains the data not explicitly mentioned in the paper such as fluxes, crossing probabilities, and probability density of states for Mg-Al and pure Mg at the aforementioned temperatures.

VI. ACKNOWLEDGMENTS

This work was supported by the National Science Foundation (NSF) under Grant No. DMR-2320355 and simulations were carried out at the Advanced Research Computing at Hopkins (ARCH) core facility, which is supported by the NSF under Grant No. OAC-1920103. We would also like to extend our gratitude to Professors Tim Weihs and Tine Curk from the Department of Material Science and Engineering at Johns Hopkins University, as well as Professor Titus van Erp from the Department of Chemistry at the Norwegian University of Science and Technology for insightful discussions and guidance.

VII. AUTHOR DECLARATIONS

A. Conflict of Interests

The authors declare that they have no known competing financial interests or personal relationships that could have appeared to influence the work reported in this paper.

B. Author Contributions

Vicente Munizaga: Investigation (lead), Computational simulations (lead), analysis (lead), Visualization (lead), Writing (equal).

Michael L. Falk: Investigation (supporting), Computational simulations (supporting), analysis (supporting), Visualization (supporting), Writing (equal).

VIII. DATA AVAILABILITY

The data that support the findings of this study are available from the corresponding author upon request.

- ¹P. Yi, M. L. Falk, and T. P. Weihs, "Suppression of homogeneous crystal nucleation of the NiAl intermetallic by a composition gradient: A molecular dynamics study," Journal of Chemical Physics **146** (2017), 10.1063/1.4982821.
- ²J. F. Nie, "Precipitation and hardening in magnesium alloys," Metallurgical and Materials Transactions A: Physical Metallurgy and Materials Science 43, 3891–3939 (2012).
- ³J. Hirsch and T. Al-Samman, "Superior light metals by texture engineering: Optimized aluminum and magnesium alloys for automotive applications," Acta Materialia 61, 818–843 (2013).
- ⁴W. J. Joost and P. E. Krajewski, "Towards magnesium alloys for high-volume automotive applications," Scripta Materialia 128, 107–112 (2017).
- ⁵E. R. In, Essential Readings in Magnesium Technology (2016).
- ⁶S. Eswarappa Prameela, P. Yi, Y. Hollenweger, B. Liu, J. Chen, L. Kecskes, D. M. Kochmann, M. L. Falk, and T. P. Weihs, "Strengthening magnesium by design: Integrating alloying and dynamic processing," Mechanics of Materials 167, 104203 (2022), arXiv:2105.05354.
- ⁷ J. Hou, X. S. Kong, X. Wu, J. Song, and C. S. Liu, "Predictive model of hydrogen trapping and bubbling in nanovoids in bcc metals," Nature Materials 18, 833–839 (2019).
- ⁸M. Zakaria and P. R. Munroe, "Void formation and morphology in NiAl," Journal of Materials Science 37, 71–79 (2002).
- ⁹F. A. Garner, "Recent insights on the swelling and creep of irradiated austenitic alloys," Journal of Nuclear Materials 122, 459–471 (1984).
- ¹⁰F. A. Garner, "Evolution of microstructure in face-centered cubic metals during irradiation," Journal of Nuclear Materials **205**, 98– 117 (1993).
- ¹¹F. A. Garner, M. B. Toloczko, and B. H. Sencer, "Comparison of swelling and irradiation creep behavior of fcc-austenitic and bccferritic/martensitic alloys at high neutron exposure," Journal of Nuclear Materials 276, 123–142 (2000).
- ¹²T. Okita, T. Kamada, and N. Sekimura, "Effects of dose rate on microstructural evolution and swelling in austenitic steels under irradiation," Journal of Nuclear Materials **283-287**, 220–223 (2000).
- ¹³M. P. Surh, J. B. Sturgeon, and W. G. Wolfer, "Master equation and Fokker-Planck methods for void nucleation and growth in irradiation swelling," Journal of Nuclear Materials 325, 44–52 (2004).
- ¹⁴S. Wu, H. S. Soreide, B. Chen, J. Bian, C. Yang, C. Li, P. Zhang, P. Cheng, J. Zhang, Y. Peng, G. Liu, Y. Li, H. J. Roven, and J. Sun, "Freezing solute atoms in nanograined aluminum alloys via high-density vacancies," Nature Communications 13, 1–11 (2022).
- ¹⁵X. Wang, C. Hatzoglou, B. Sneed, Z. Fan, W. Guo, K. Jin, D. Chen, H. Bei, Y. Wang, W. J. Weber, Y. Zhang, B. Gault, K. L. More, F. Vurpillot, and J. D. Poplawsky, "Interpreting nanovoids in atom probe tomography data for accurate local

- compositional measurements," Nature Communications 11, 1-11 (2020).
- ¹⁶P. Yi, T. T. Sasaki, S. Eswarappa Prameela, T. P. Weihs, and M. L. Falk, "The interplay between solute atoms and vacancy clusters in magnesium alloys," Acta Materialia **249**, 118805 (2023).
- ¹⁷J. J. Laidler and B. Mastel, "Nucleation of voids in irradiated stainless steel," Nature 239, 97–98 (1972).
- ¹⁸K. C. Russell, "Vacancy cluster: Helium synergy in void nucleation," Metallurgical and Materials Transactions A: Physical Metallurgy and Materials Science 39 A, 956–963 (2008).
- ¹⁹S. Rokkam, A. El-Azab, P. Millett, and D. Wolf, "Phase field modeling of void nucleation and growth in irradiated metals," Modelling and Simulation in Materials Science and Engineering 17, 0–18 (2009).
- ²⁰K. Kelton and A. L. Greer, Nucleation in Condensed Matter: Applications in Materials and Biology (Elsevier, 2016).
- ²¹D. Kumar and S. Ray, "Void nucleation as a diffusive instability," Phys. Rev. B **34**, 5048–5057 (1986).
- ²²D. Peak and J. W. Corbett, "The effect of spatial correlations on steady-state nucleation kinetics in dense fluid systems," Journal of Statistical Physics 17, 97–110 (1977).
- ²³D. Peak and J. W. Corbett, "The effect of spatial correlations on the steady state nucleation of voids," Radiation Effects 36, 197–203 (1978).
- ²⁴G. M. Torrie and J. P. Valleau, "Monte Carlo free energy estimates using non-Boltzmann sampling: Application to the subcritical Lennard-Jones fluid," Chemical Physics Letters 28, 578–581 (1974).
- ²⁵ A. Laio and M. Parrinello, "Escaping free-energy minima," Proceedings of the National Academy of Sciences of the United States of America 99, 12562–12566 (2002), arXiv:0208352 [cond-mat].
- ²⁶A. F. Voter, "A method for accelerating the molecular dynamics simulation of infrequent events," Journal of Chemical Physics 106, 4665–4677 (1997).
- ²⁷T. S. Van Erp, D. Moroni, and P. G. Bolhuis, "A novel path sampling method for the calculation of rate constants," Journal of Chemical Physics 118, 7762–7774 (2003), arXiv:0210614 [cond-mat].
- ²⁸T. S. van Erp and P. G. Bolhuis, "Elaborating transition interface sampling methods," Journal of Computational Physics **205**, 157– 181 (2005), arXiv:0405116 [cond-mat].
- ²⁹P. G. Bolhuis, "Transition-path sampling of β -hairpin folding," Proceedings of the National Academy of Sciences of the United States of America **100**, 12129–12134 (2003).
- 30 P. G. Bolhuis, "Kinetic pathways of β -hairpin (un)folding in explicit solvent," Biophysical Journal 88, 50–61 (2005).
- ³¹M. Moqadam, A. Lervik, E. Riccardi, V. Venkatraman, B. K. Alsberg, and T. S. Van Erp, "Local initiation conditions for water autoionization," Proceedings of the National Academy of Sciences of the United States of America 115, E4569–E4576 (2018).
- ³²A. Arjun and P. G. Bolhuis, "Rate Prediction for Homogeneous Nucleation of Methane Hydrate at Moderate Supersaturation Using Transition Interface Sampling," Journal of Physical Chemistry B 124, 8099–8109 (2020).
- ³³Y. Liang, G. Díaz Leines, R. Drautz, and J. Rogal, "Identification of a multi-dimensional reaction coordinate for crystal nucleation in Ni3Al," The Journal of chemical physics 152, 224504 (2020).
- ³⁴G. Díaz Leines, R. Drautz, and J. Rogal, "Atomistic insight into the non-classical nucleation mechanism during solidification in Ni," Journal of Chemical Physics 146, 1–10 (2017).
- ³⁵M. GrÜnwald and C. Dellago, "Transition path sampling studies of solid-solid transformations in nanocrystals under pressure," in *Trends in Computational Nanomechanics: Transcending Length* and *Time Scales*, edited by T. Dumitrica (Springer Netherlands, Dordrecht, 2010) pp. 61–84.
- ³⁶A. Lervik, I. H. Svenum, Z. Wang, R. Cabriolu, E. Riccardi, S. Andersson, and T. S. van Erp, "The role of pressure and defects in the wurtzite to rock salt transition in cadmium selenide,"

- Physical Chemistry Chemical Physics, 8378–8386 (2022).
- ³⁷T. S. Van Erp, "Reaction rate calculation by parallel path swapping," Physical Review Letters 98, 1–4 (2007), arXiv:0704.3317.
- ³⁸K. E. Blow, D. Quigley, and G. C. Sosso, "The seven deadly sins: When computing crystal nucleation rates, the devil is in the details," Journal of Chemical Physics **155** (2021), 10.1063/5.0055248, arXiv:2104.13104.
- ³⁹S. Plimpton, "Fast parallel algorithms for short-range molecular dynamics," Journal of Computational Physics 117, 1–19 (1995).
- ⁴⁰Y.-M. Kim, N. J. Kim, and B.-J. Lee, "Atomistic modeling of pure mg and mg-al systems," Calphad 33, 650-657 (2009).
- ⁴¹M. Tuckerman, B. J. Berne, and G. J. Martyna, "Reversible multiple time scale molecular dynamics," The Journal of Chemical Physics 97, 1990–2001 (1992).
- ⁴²M. Parrinello and A. Rahman, "Polymorphic transitions in single crystals: A new molecular dynamics method," Journal of Applied Physics **52**, 7182–7190 (1981).
- ⁴³G. J. Martyna, D. J. Tobias, and M. L. Klein, "Constant pressure molecular dynamics algorithms," The Journal of Chemical Physics **101**, 4177–4189 (1994).
- ⁴⁴W. Shinoda, M. Shiga, and M. Mikami, "Rapid estimation of elastic constants by molecular dynamics simulation under constant stress," Physical Review B - Condensed Matter and Materials Physics 69, 16–18 (2004).
- ⁴⁵A. Stukowski, "Visualization and analysis of atomistic simulation data with ovito—the open visualization tool," Modelling and Simulation in Materials Science and Engineering 18, 015012 (2009).
- ⁴⁶C. Dellago, P. G. Bolhuis, and P. L. Geissler, "Transition Path Sampling Methods," in *Lecture Notes in Physics, Berlin*

- Springer Verlag, Vol. 1, edited by M. Ferrario, G. Ciccotti, and K. Binder (2006) p. 349.
- ⁴⁷J. Rogal, W. Lechner, J. Juraszek, B. Ensing, and P. G. Bolhuis, "The reweighted path ensemble," Journal of Chemical Physics 133 (2010), 10.1063/1.3491817.
- ⁴⁸A. M. Ferrenberg and R. H. Swendsen, "Optimized monte carlo data analysis," Phys. Rev. Lett. **63**, 1195–1198 (1989).
- ⁴⁹E. Riccardi, A. Lervik, S. Roet, O. Aarøen, and T. S. van Erp, "PyRETIS 2: An improbability drive for rare events," Journal of Computational Chemistry 41, 370–377 (2020).
- ⁵⁰D. Frenkel and B. Smit, "Chapter 5 monte carlo simulations in various ensembles," in *Understanding Molecular Simulation* (Second Edition), edited by D. Frenkel and B. Smit (Academic Press, San Diego, 2002) second edition ed., pp. 111–137.
- ⁵¹P. G. Bolhuis, "Rare events via multiple reaction channels sampled by path replica exchange," Journal of Chemical Physics 129, 1–13 (2008).
- ⁵²S. W. Hall, G. Díaz Leines, S. Sarupria, and J. Rogal, "Practical guide to replica exchange transition interface sampling and forward flux sampling," Journal of Chemical Physics **156** (2022), 10.1063/5.0080053.
- ⁵³T. Sasaki, J. Lin, P. Yi, Z. Li, S. Prameela, A. Park, E. Lipkin, A. Lee, M. Falk, T. Weihs, and K. Hono, "Deformation induced solute segregation and G.P. zone formation in Mg-Al and Mg-Zn binary alloys," Scripta Materialia 220, 114924 (2022).